We are IntechOpen, the world's leading publisher of Open Access books Built by scientists, for scientists

4,800
Open access books available

122,000
International authors and editors

135M
Downloads

Our authors are among the

154
Countries delivered to

TOP 1%
most cited scientists

12.2%
Contributors from top 500 universities

WEB OF SCIENCE™

Selection of our books indexed in the Book Citation Index in Web of Science™ Core Collection (BKCI)

Interested in publishing with us?
Contact book.department@intechopen.com

Numbers displayed above are based on latest data collected.
For more information visit www.intechopen.com

20

Recent Advances in Modelling and Simulation of Silicon Photonic Devices

Vittorio M. N. Passaro and Francesco De Leonardis
Photonics Research Group, Dipartimento di Elettrotecnica ed Elettronica, Politecnico di Bari
Italy

1. Introduction

Nowadays, the interest for a large number of topics in Photonics research field is very high and of increasing importance (Reed, 2004), (Reed & Knights, 2004). A very important Silicon technology Company as Intel Corp. is developing many research programs in Photonics, with the aim to use silicon as a fundamental technological platform for all the photonic functions in any telecommunications system link (including generation, modulation, filtering, wavelength conversion, switching, amplification and detection of light). In fact, silicon low cost, vast existing microelectronics infrastructure and its technology allowing large integration of electronic and photonic devices, make Silicon-on-Insulator (SOI) technological platform a very attractive prospective for Photonics. Silicon photonics most promising applications are in the fields of optical interconnects, low-cost telecommunications and optical sensors. Optical interconnects have been demonstrated as very important because they permit to achieve a significant bandwidth increase in a variety of application areas including rack-to-rack, board-to-board, chip-to-chip and intrachip applications. SOI optical interconnects may permit to overcome the bandwidth limitations due to frequency-dependent losses imposed by copper interconnects.
Actually, employment of electronic and optical micro- and nano-sensors in a great number of application fields such as medicine, microbiology, particle physics, automotive, environmental safety and defence is receiving an increasing interest. Sensor and actuator monolithic integration in micro-electro-mechanical systems (MEMSs), nano-electro-mechanical systems (NEMSs) and micro-opto-electro-mechanical systems (MOEMSs) has been achieved in a great number of sensing devices. Photonic sensors have attracted a great attention because of their immunity to electromagnetic interference, good compactness and robustness and high compatibility with fibre networks, but also because they usually exhibit shorter response time and higher sensitivities with respect to MEMS/MOEMS devices. Different integrated optical chemical and biochemical sensors have been proposed adopting prevalently CMOS-compatible technological platforms.
Thus, the tasks of modelling and simulation of photonic devices and systems is becoming as more and more significant. However, a large number of modelling techniques for Photonics is not yet well standardized and many aspects of simulation tasks are still open. In general, different well known modelling techniques include beam propagation methods (BPM),

finite difference time domain (FDTD), as well as coupled mode theory (CMT), transfer matrix methods (TMM), Floquet-Bloch theory (FBT) for periodic structures (Passaro, 2000) and method of lines (MoL) (Scarmozzino et al., 2000). Powerful commercial CAD tools are often used in literature, as those produced by Silvaco Corp., Apollo Photonics Inc., Optiwave Systems Inc., RSoft Design Group.

In this frame, the Photonics Research Group of Politecnico di Bari (URL: http://dee.poliba.it/photonicsgroup) is very active and internationally recognized for modelling and simulation of photonic devices and systems. Along many years, it has developed a number of home-made modelling techniques and numerical approaches to design and simulate various devices, including grating-assisted directional couplers, optical modulators, thermo-optic devices, photonic sensors, nonlinear devices and so on.

In this chapter we review recently developed simulation methods for sub-micrometer innovative SOI guiding structures and photonic devices. Techniques based on full-vectorial finite element method (FV-FEM) for modal and sensitivity analysis of silicon slot waveguides will be described in detail, showing as these guiding structures can be made extremely sensitive to sensing medium refractive index shift. Some properties of an innovative novel photonic structure, the hollow waveguide, will be also given. Multiphysics modelling techniques enabling to contextually simulate many physical phenomena taking place within a device have been demonstrated as very useful in a wide spectrum of silicon photonic device modelling. We will also describe how, in a unique simulation environment, it is possible to simulate either optical and electronic phenomena that takes place in SOI photonic modulators or thermal and optical effects characterizing the performance of silicon thermo-optic devices. Finally, some aspects of modelling of nonlinear photonic devices in SOI will be also considered, with emphasis on generation of optical solitons.

2. Numerical results

2.1 Silicon waveguides

Recently, SOI sub-micrometer wire waveguides (Yamada et al., 2006) have been demonstrated very attractive for integrated optical sensors, because they exhibit a sensitivity significantly larger than in other guiding structures based on silicon oxinitride (SiON), or polymeric materials or silica.

When two Si-wires are very close to each other, it is possible to realize another important SOI nanometer guiding structure, usually known as SOI slot waveguide (Xu et al., 2004)]. A great variety of optical devices has been recently proposed or fabricated by using slot waveguides, including microring resonators, optical modulators, electrically pumped light emitting devices, directional couplers, all-optical logic gates and beam splitters. Moreover, a full-vectorial finite element method (FV-FEM) modal investigation devoted to study the influence of slot waveguide geometrical parameters on optical power fraction confined in the low-index gap region has been also carried out (Muellner & Heinberger, 2006), (Dell'Olio & Passaro, 2007). In this section, some results of SOI slot waveguides are briefly reviewed as obtained by a commercial CAD tool, FEM by COMSOL Multiphysics.

Conventional SOI slot waveguide (whose structure is shown in Fig. 1(a)) has a typical modal behaviour, assuming as cover medium air, silicon oxide or an aqueous solution (cover medium refractive index n_c equal to 1, 1.444 or 1.33 at wavelength 1550 nm, respectively). In FEM mesh generation for effective index and modal profile calculation, triangular vector-elements have been used and maximum element size fixed as equal to 2.5 nm in the gap

region, 3 nm in the Si wires region, 10 nm in the portion of calculation domain outside both gap region and Si wires region and included in a large rectangle 1 μm wide and 0.45 μm high centred in the centre of the gap region, and 100 nm in the remaining domain portion having a total area of 8 μm² (4μm × 2 μm). In total, about 100,000 mesh elements have been always used. Changing the boundary condition from a perfect electric conductor to a perfect magnetic conductor is demonstrated to have a negligible influence on the simulation results. Adopting these mesh parameters, the slot waveguide fabricated by (Xu et al., 2004) has been simulated. Calculated effective indices (1.757767 for quasi-TM mode and 1.611924 for quasi-TE at the operating wavelength of 1545 nm) are very similar with those experimentally measured, the relative change being lower than 1 %.

Slot guiding structure supports both a quasi-TE mode, highly confined in the gap region as in Fig. 1(b), and a quasi-TM mode too, as in Fig. 1(c). Moreover, slot waveguide fabrication implies silicon deep etching that, in principle, can produce non vertical side-walls, as depicted in Fig. 1(d). Waveguide modal profiles, either for quasi-TE or quasi-TM modes, are significantly influenced by this kind of fabrication tolerance, as it can be seen in Fig. 1(d) and Fig. 1(e), respectively. Thus, non vertical sidewall effect on conventional SOI slot waveguide modal properties has been also investigated by FV-FEM.

Assuming silicon wires with height h =250 nm, width w =180 nm and gap region width g=100 nm, the effective index change as induced by non vertical sidewalls with respect to vertical case, has been calculated. Tilting angle θ as sketched in Fig. 1 (d) with respect to vertical direction has been varied in the range from 3° to 9°, and quasi-TE and quasi-TM modes have been calculated (see Fig. 2). A linear dependence of effective index change on the tilting angle θ has been observed for both polarizations. Non vertical sidewalls influence on effective index is stronger for quasi-TE than for quasi-TM mode, because the relevant electric field squared module has its maxima along the vertical interfaces between silicon wires and gap region for quasi-TE mode, while the maxima are outside the gap region for quasi-TM mode. An increase of cover medium refractive index (from air to silicon oxide) will produce a decrease of θ influence on effective index, as it is shown in Fig. 2.

Considering θ = 8°, g = 100 nm and h = 250 nm, the effective index change induced by non vertical sidewalls has been investigated as a function of w for quasi-TE and quasi-TM modes (Fig. 3). If the cover medium is silicon oxide or an aqueous solution, this change monotonically decreases with increasing the silicon wire width. When cover medium is air, the dependence of effective index shift on w exhibits a maximum for w = 180 nm (maximum values are 20.5 % and 6.15% for quasi-TE and quasi-TM mode, respectively).

The confinement factors in the cover medium Γ_C and in the gap region Γ_G for quasi-TE and quasi-TM modes propagating in slot waveguide can be defined as:

$$\Gamma_C = \frac{\iint_C |\mathbf{E}(x,y)|^2 \, dxdy}{\iint_\infty |\mathbf{E}(x,y)|^2 \, dxdy} \qquad \Gamma_G = \frac{\iint_G |\mathbf{E}(x,y)|^2 \, dxdy}{\iint_\infty |\mathbf{E}(x,y)|^2 \, dxdy} \tag{1}$$

where **E**(x,y) is the electric field vector and *C* and *G* indicate cover medium and gap region, respectively, being the gap region a part of cover medium region, as shown in Fig. 1 (a).

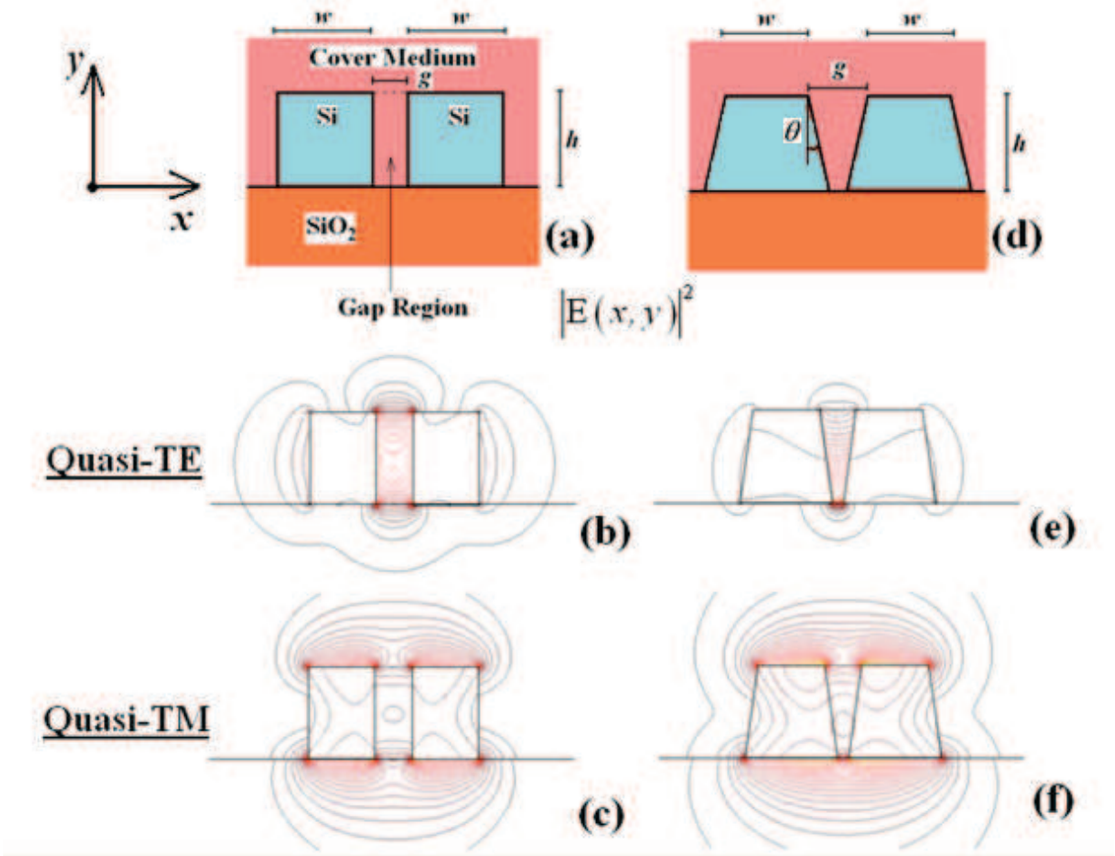

Figure 1. (a) Conventional SOI slot waveguide structure with vertical sidewalls (θ=0°). (b-c) Relevant electric field squared module for quasi-TE and quasi-TM optical modes. (d) SOI slot waveguide with non vertical sidewalls (θ = 8°). (e-f) Relevant electric field squared module for quasi-TE and quasi-TM optical modes. For these graphs, an aqueous solution (n_c =1.33) is assumed as cover medium (h = 250 nm, w = 180 nm, g =100 nm)

Dependence of confinement factors Γ_C and Γ_G on w can be investigated for g=100 nm and h=250 nm. Effect of non vertical sidewalls (θ=8°) on these factors has been also considered. The confinement factors are larger for quasi-TE than for quasi-TM mode. For quasi-TE mode, non vertical sidewalls produce a decrease in Γ_C and an increase in Γ_G. For quasi-TM mode, non vertical sidewalls produce a decrease of both confinement factors.

For both polarizations, when the cover medium is an aqueous solution or silicon oxide, Γ_C monotonically decreases when w increases, while Γ_C exhibits a maximum when the cover medium is air. Confinement factor Γ_G has a maximum in quite all considered cases (only when we consider silicon oxide, non vertical sidewalls and quasi-TM mode, Γ_G dependence on w is monotone). These results are very important for design of optimal slot waveguides for sensing purposes.

Another important CMOS-compatible technology involves the use of hollow optical waveguides (Harrington, 2000). Calculations of effective indices and field distributions are again carried out by FV-FEM with 10,000 mesh elements. In Fig. 4 the electric field x-component of fundamental mode is sketched for a 4x4 μm² squared core structure, having six periods of silicon/silicon nitride all around (effective index 1.438571 in figure). The plot

shows as the mode confinement occurs in the center low index region (silicon oxide in this case), if a grating at resonance wavelength is fabricated all around. The grating can have a variable number of periods, each one being formed in this case by one layer of silicon and one layer of silicon nitride. The thickness of each layer must be designed in order to meet the Bragg condition for that wavelength (i.e. λ = 1.55μm), thus silicon layers are ~110 nm thick, and silicon nitride layers are ~194 nm thick. Table 1 summarizes the effective indices for structures with different number of periods. We can note that, starting from at least three periods (three silicon layers), the field confinement is good and losses are expected to be as moderate.

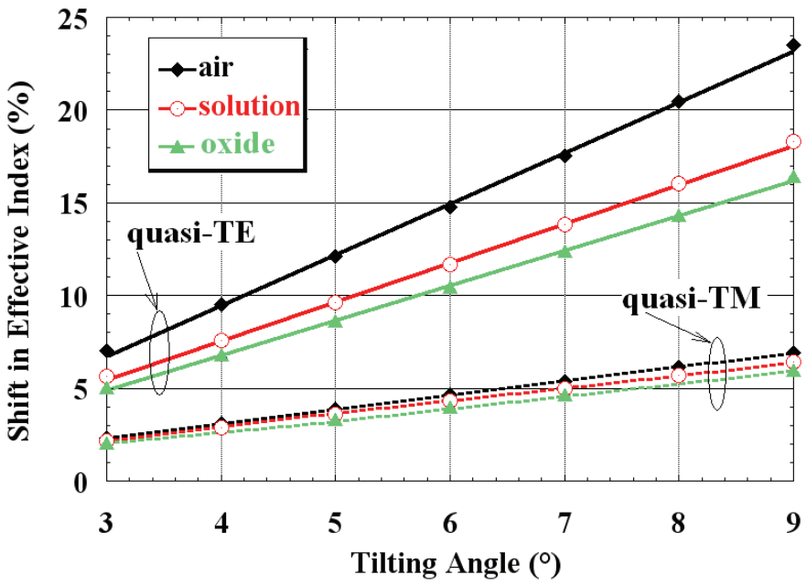

Figure 2. Percentage shift of quasi-TE and quasi-TM mode effective indices, with respect to vertical case, versus θ (h = 250 nm, w = 180 nm, g=100 nm), for various cover materials

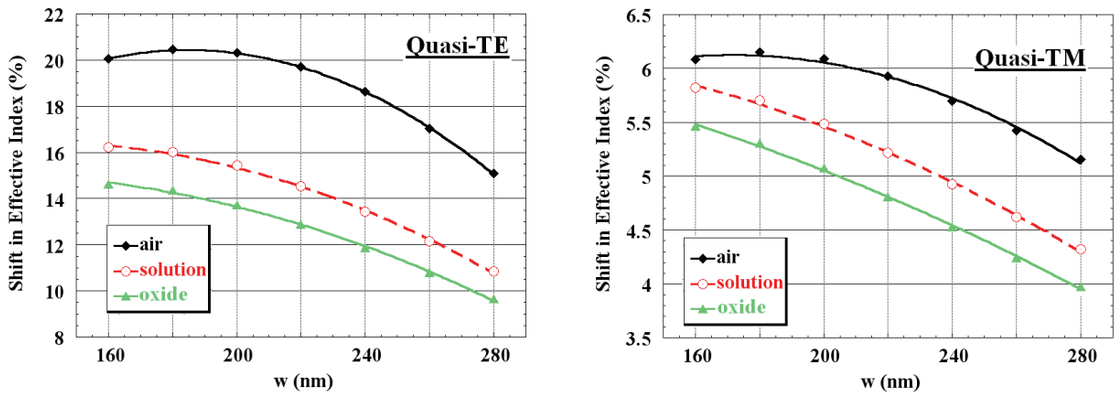

Figure 3. Percentage shift of quasi-TE and quasi-TM mode effective indices (with respect to vertical case) versus w, as induced by non vertical sidewalls in slot waveguides (h = 250 nm, g =100 nm, θ = 8°)

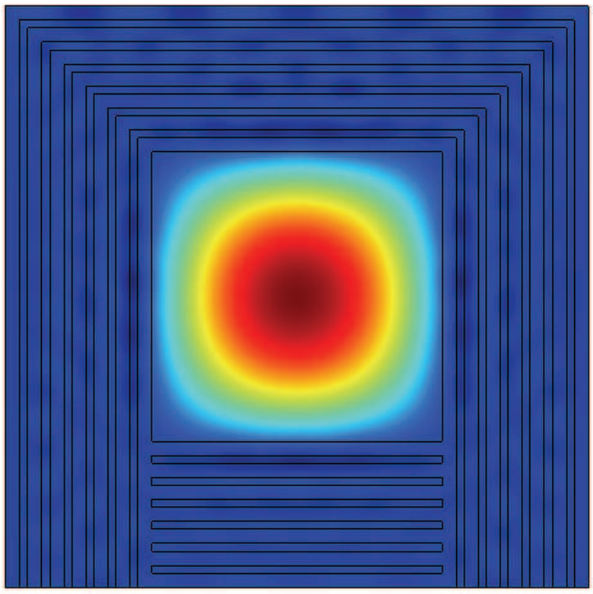

Figure 4. Electric field x-component plot for field confinement in hollow waveguide

Structure	Effective index n_{eff} x-component	Effective index n_{eff} y-component
6 periods	1.438571	1.438567
5 periods	1.438581	1.438596
4 periods	1.438636	1.438654
3 periods	1.439916	1.438956
2 periods	1.440526	1.440403
1 period	1.437340	1.437340

Table 1. Effective indices (squared core) versus number of periods for both polarizations

2.2 Thermo-optic devices

Recently, there has been also a great interest in the development of optical waveguide modulators, switches, ring resonators, filters, couplers using silicon-on-insulator (SOI) technology (Passaro, 2006). SOI-based optical devices are characterized by small optical losses over telecommunication wavelengths and have the potential for integration with SOI-based CMOS electronics, reduced parasitics, absence of latch-up and enabling high-speed operation at low power.

One significant technological issue is associated with the ability to perform optical modulation. An attractive way to modulate the refractive index in SOI rib waveguides is the thermo-optic effect, allowing low transmission loss, low cost, high stability, low power consumption and very large scale of integration. Apart from the well known optical characteristics, silicon also possesses good thermal features, with its high thermo-optical coefficient and thermal conductivity. Both static and dynamic thermo-optical analysis of small rib waveguides can be carried out by FV-FEM. In this section, we briefly review the

fully integrated thermo-optic simulation where both thermal and optical investigations, without approximations on the refractive index distribution and consequently on effective indices of structure modes, can be carried out. Typically, the two analysis are developed in literature in two different simulation environments, so requiring some methods to export the refractive index distribution and introducing approximations.
Thermo-optic effect in SOI rib waveguides can be appropriately simulated by considering an aluminum heater laying on the top of the structure. The finite element method has been used to solve both thermal and wave propagation problems in rib optical waveguides, at the wavelength of 1.55μm. The thermal problem is solved and the obtained temperature distribution is used to evaluate the refractive index change in the heated regions, caused by the thermo-optic effect. This distribution of refractive index is then used to solve the optical problem. The analysis of waveguides is carried out in the x-y plane, perpendicular to the light propagation direction z. The mathematical equation for heat transfer by conduction is the heat equation:

$$\rho C \frac{\partial T}{\partial t} + \nabla \cdot \left(-k \nabla T \right) = Q \tag{2}$$

where T is the temperature (K), Q is a heat source or heat sink (W/m^3), ρ is the density (kg/m^3), C is the heat capacity (J/kg·K) and k is the thermal conductivity (W/m·K) of the medium. These three thermo-physical properties determine the thermal diffusivity a (m^2/s), which gives information on how rapidly a temperature variation at the medium surface propagates through the medium itself. If the thermal conductivity is isotropic, equation (2) becomes:

$$\rho C_p \frac{\partial T}{\partial t} - k \nabla^2 T = Q \tag{3}$$

In a stationary problem, the temperature does not change with time and the first term of the equation disappears. If there is not heat production or consumption in the medium, Q sets to zero. To solve a particular heat conduction problem and find the temperature distribution inside a medium, it is necessary to specify the medium geometry and thermo-physical properties, the distribution of possible sources and the initial and boundary conditions. These conditions are essentially of two types: Dirichlet, where temperature is imposed on the medium surface as $T = T_0$, or Neumann, where the heat flux $\boldsymbol{q}$ on a boundary is $-\boldsymbol{n} \cdot \boldsymbol{q} = q_0$ and $\boldsymbol{n}$ stands for the surface normal. The heat flux is defined by the Fourier law as $\boldsymbol{q} = -k \nabla T$, where the negative sign is justified by the opposite directions of heat flux and temperature gradient. Moreover, light propagation is described by the optical wave equation:

$$\nabla^2 \mathrm{E_t} + \nabla \left(\frac{\nabla n^2 (x,y) \times \mathrm{E_t}}{n^2 (x,y)} \right) + \left(\frac{2\pi}{\lambda} \right)^2 n^2 (x,y) \mathrm{E_t} = \left(\frac{2\pi}{\lambda} \right)^2 n_{eff} \mathrm{E_t} \tag{4}$$

derived from Maxwell's equations, where E_t is the transverse electric field, λ is the wavelength, n(x,y) is the refractive index distribution and n_{eff} is the effective index (wave

equation eigenvalue).
It is well known as SOI waveguides typically have a silicon core (refractive index n ~3.5) surrounded by cladding layers of air or silica, with refractive indices between 1 and 2. Hence, the very high index contrast between waveguide core and cladding allows good confinement of optical modes and reduction of device dimensions. A typical SOI rib waveguide is sketched in Fig. 5, with an aluminum heater on the top, having a width *W*. The buried oxide (BOX) layer is required to achieve thermal isolation of the waveguide from the substrate, because the thermal conductivity in SiO_2 is about 100 times smaller than in silicon. The distance H between the heater and the top of the rib must be thick enough to insulate the waveguide core from the metallic electrode. For all the analyzed structures we have set this distance to 0.1μm, being the buried oxide thickness of 1μm.

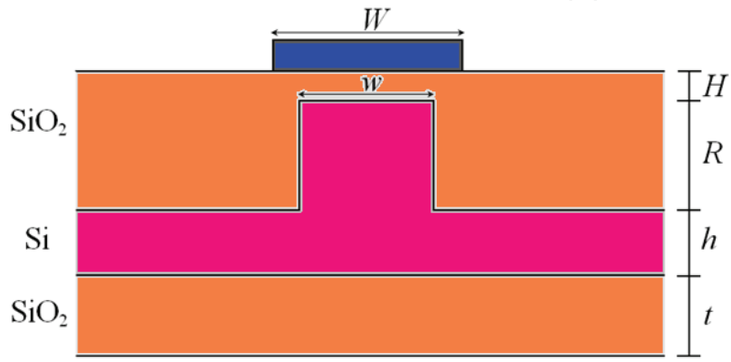

Figure 5. General view of SOI rib waveguide with the heater on the top

We have considered the absence of any thermal generation terms and a scalar conductivity for both static and dynamic analysis. Table 2 collects the thermo-physical values used in the simulations for the materials involved in the waveguide. As initial condition, a constant temperature T_0 has been set at each point of the structure. The boundary conditions are:

$T = T_0$ on the top and bottom boundary

$T = T_{heater}$ on heater surfaces

$\boldsymbol{n}\cdot\left(k\nabla T\right) = 0$ on lateral surfaces

$\boldsymbol{n}\cdot\left(k_1\nabla T_1 - k_2\nabla T_2\right) = 0$ on internal boundaries

where T_{heater} becomes a temperature step in the dynamic analysis, and a constant value in the static analysis. In both cases, the maximum heater temperature change is assumed as 70°C. The 2D temperature distribution obtained in the thermal investigation has been used to evaluate the new refractive indices of the waveguide, as a result of the thermo-optic effect in silicon (n'_{Si}=3.477+1.86×10$^{-4}\Delta T$) and in silica ($n'_{SiO_2} = 1.477 + 10^{-5}\Delta T$), at the wavelength 1.55μm. ΔT is the temperature change caused by heating and the bulk thermo-optic coefficients of silicon and silica are used. The refractive index distribution is taken to solve the eigenvalue optical problem and evaluate the field distributions and the effective indices of the structure modes.
By means of the static analysis, performed at various temperatures of the heater, the dependence of the effective indices on temperature can be derived as an *effective* thermo-optic coefficient, $\partial n_{eff}/\partial T$. This procedure is significantly different from that commonly

followed in literature, where only the bulk thermo-optic coefficient is usually considered. Of course, this effective thermo-optic coefficient depends on waveguide materials (refractive index, density, heat capacity, thermal conductivity), geometry, temperature gradient in each layer, heater material and width.

Material	k W/m·K	P kg/m³	C J/kg·K
silicon	163	2330	703
silica	1.38	2203	703
aluminum	160	2700	900
Air (@ 30°C)	0.026	1.166	1005

Table 2. Thermo-physical constants used in simulations

If a guided-wave optical device employs the thermo-optic effect for switching, filtering or tuning functions, its characteristics and properties will depend on this effective thermo-optic coefficient, that can be seen as a property of the whole guided-wave structure. For example, in a Mach-Zehnder thermo-optic switch, the phase shift is written as:

$$\Delta\varphi = \frac{2\pi}{\lambda}\Delta n_{eff} L_h = \frac{2\pi}{\lambda} L_h \frac{\partial n_{eff}}{\partial T}\Delta T \tag{5}$$

where L_h is the heater length. In the results, rib waveguides with sizes $h+R=1\mu m$, $w=0.6\mu m$, $R=0.6\mu m$, and $W=0.6\mu m$ have been considered. Then, etch depth R and h (keeping the sum h+R as constant), waveguide width w and heater width W have been changed, and derived their influence on the effective index. Fig. 6 shows the linear dependence of effective index change over heater temperature for both polarizations (quasi-TE and quasi-TM), for waveguides with different etch depth R.

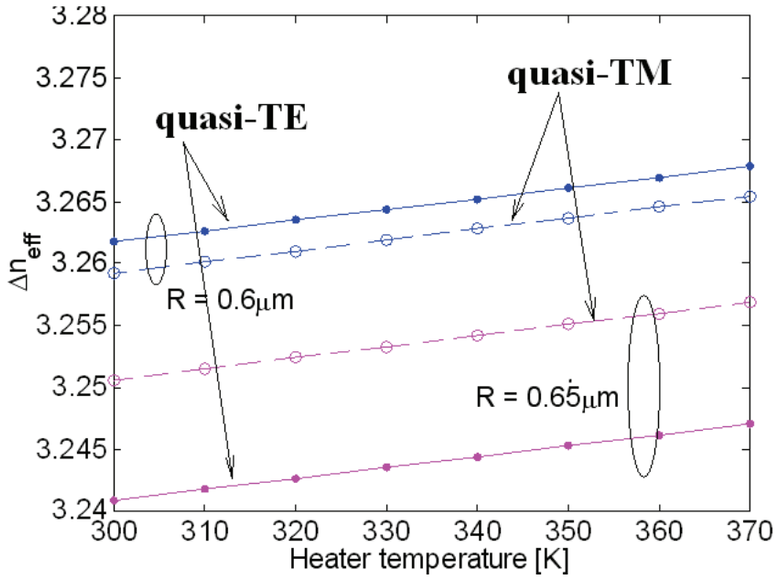

Figure 6. Effective index change versus heater temperature

By means of the dynamic analysis, the time dependence of effective index can be found, so estimating the thermo-optic response time of the analyzed structures. The time constant τ of the thermo-optic effect for each considered structure has been evaluated and fitted by an exponential law, as sketched in Fig. 7. The time constant gets better in structures where the effective thermo-optic coefficient is improved too. Furthermore, the time constant and the thermo-optic coefficient are always improved when considering quasi TM mode instead of quasi-TE, because in that case the field maximum is placed in a more heated region. Time constants ranging from 0.93 μs to 0.85 μs have been determined with changing the rib etch depth from 0.6 to 0.7 μm.

Thus, by means of this fully integrated multiphysics analysis, we have avoided the approximation of constant thermo-optic coefficients in the waveguide layers, as usually assumed in literature. This is especially important in the core of the waveguide, where the field intensity is maximum.

Furthermore, our rigorous approach is crucial, especially for operating with waveguides where the guiding layer is constituted of materials with low thermal diffusivity. The importance of the diffusivity can be highlighted in the study of a waveguide where silica is placed over the heater instead air. Both static and dynamic behaviors get better, because the diffusivity of silica is approximately two orders of magnitude lower than for air. Thus, the thermal power could be better confined in the guiding layer.

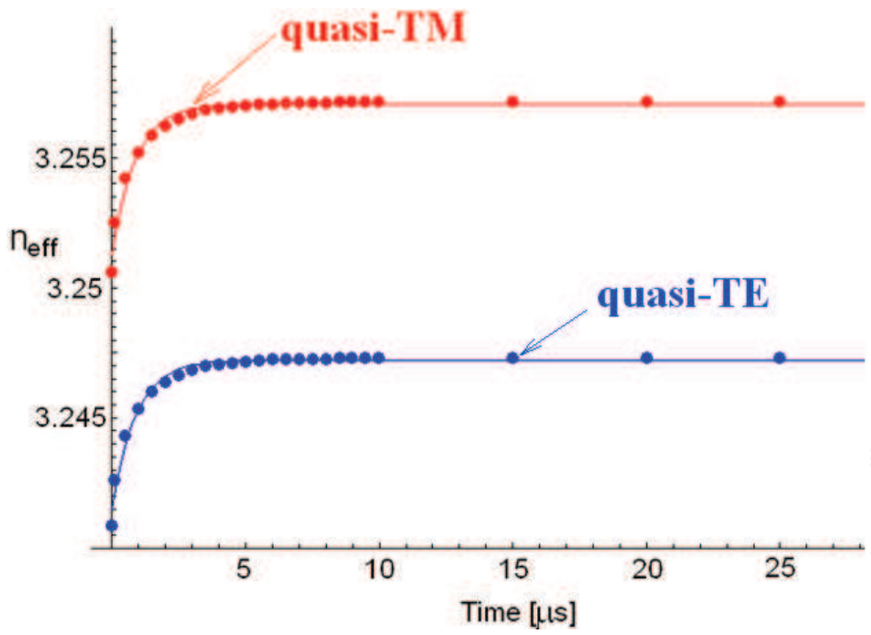

Figure 7. Time response for quasi-TE and quasi-TM modes

2.3 Silicon modulators

One of the most important requirements of any integrated optical technology is the ability to perform optical modulation, which permits to encode a bit steam onto the optical carrier provided by the laser source. Light can be modulated using different physical effects, depending on the material used to fabricate modulators. For high-speed modulation, electro-optic effect is commonly employed.

Unfortunately, unstrained silicon does not exhibit this physical effect, thus the plasma dispersion effect is commonly used to solve the problem of optical modulation. It is based on inducing an electrically change of silicon refractive index by varying electron and hole distributions within the material. The free-carrier concentration in silicon electro-optic devices can be varied by charge carrier injection, accumulation or depletion. In literature p-i-n, p-n (see Fig. 8a) and metal-oxide-semiconductor (MOS) (see Fig. 8b) structures have been adopted to this purpose.

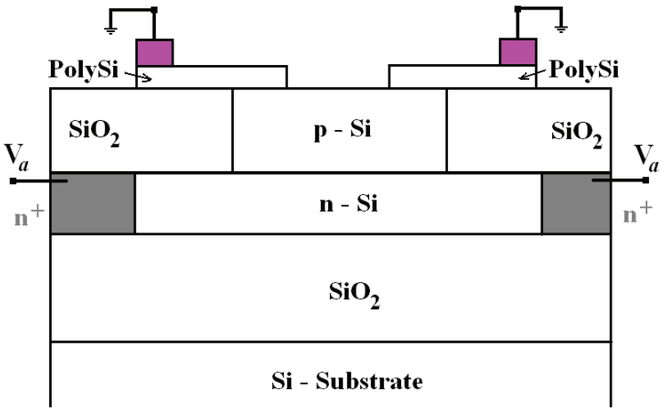

(a)

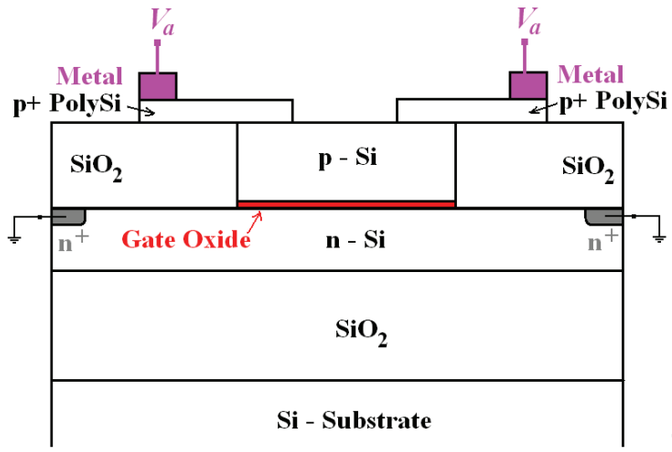

(b)

Figure 8. Typical structures for silicon modulators: (a) p-n; (b) MOS

To study this kind of devices, two different models are usually developed. The first allows to investigate the modulator electrical behaviour, whereas the second simulates the device from an optical point of view, taking into account the electrically induced silicon refractive index change (Barrios & Lipson, 2004). Usually, these two models are developed in literature by all authors in two different simulation environments, the former purely electrical and the latter purely optical, giving some consequent problems and inaccuracies in using the electrical simulation results in the environment where optical simulation is performed. In this section, the fully integrated FEM-based optoelectronic model of a SOI optical modulator is briefly reviewed, assuming a typical MOS structure, as in Fig. 9.

Assuming to ground n-type silicon layer, a free carrier thin layer is accumulated on both sides of gate oxide, when a positive voltage V_a, larger than the MOS flat band voltage, is applied to the device. According with plasma-optic effect, this voltage-induced free carrier accumulation locally changes the silicon refractive index. This operating principle allows high modulation speeds to be achieved, because no slow phenomena are involved in the accumulation process. The electrically induced localized change of silicon refractive index affects the effective index of optical mode propagating within modulator and, finally, the phase of optical signal passing through it. The phase shift can be converted as an amplitude modulation using the typical Mach-Zehnder interferometer architecture.

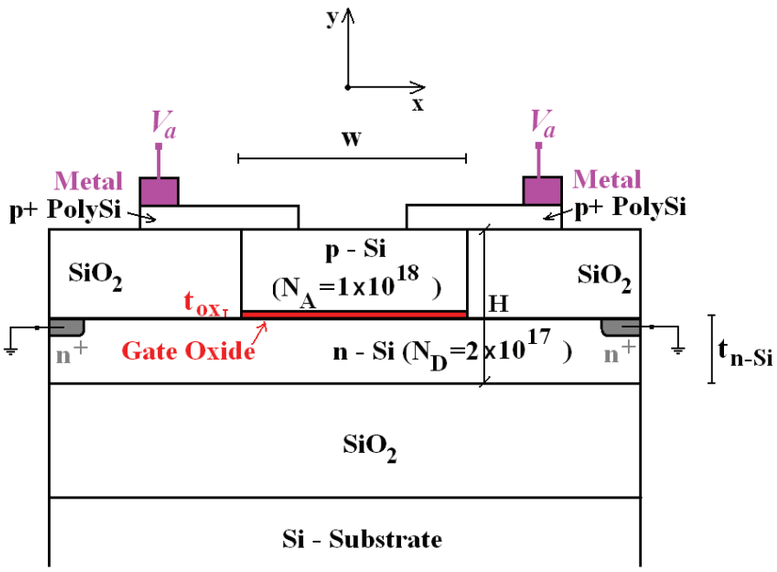

Figure 9. Simulated SOI modulator cross section (dopant concentrations in cm-3)

In our modeling we have assumed device sizes and simulation parameters as summarized in Table 3. Electron and hole distribution dependence on applied voltage (V_a) has been investigated using 2D static drift-diffusion model, solved by FEM.

Parameter	Symbol	Value
p-Si region width	w	1600 nm
modulator total height	H	1550 nm
n-Si region thickness	$t_{n\text{-}Si}$	900 nm
gate oxide thickness	t_{ox}	10.5 nm
operating wavelength	λ	1550 nm

Table 3. Modulator sizes and simulation parameters

This model consists of three coupled partial differential equations (PDEs) in the form:

$$\varepsilon_0 \varepsilon_r \left(\nabla \Psi\right) = q\left(N_e - N_h - C\right) \tag{6}$$

$$\nabla \bullet \left(\mu_p v_T \nabla N_h + \mu_p N_h \nabla \Psi\right) = R_{SRH} \tag{7}$$

$$\nabla \bullet \left(\mu_n v_T \nabla N_e - \mu_n N_e \nabla \Psi\right) = R_{SRH} \tag{8}$$

where R_{SHR} is the Shockley-Hall-Read recombination rate:

$$R_{SHR} = \frac{N_e N_h - N_i^2}{\tau_p \left(N_e + N_i\right) + \tau_n \left(N_h + N_i\right)} \tag{9}$$

and ε_0 is the vacuum permittivity, ε_r is the relative permittivity, q is the elementary charge, N_e is the electron distribution, N_h is the hole distribution, N_i is the silicon free-carrier intrinsic concentration, C is the doping profile, μ_n is the electron mobility, μ_p is the hole mobility, v_T is the thermal voltage, ψ is the electro-static potential, τ_n is the electron lifetime in silicon and τ_p is the hole lifetime in silicon.

For boundaries in contact with air, normal components of electric displacement and current density vectors are imposed to be equal to zero. At boundaries in contact with a metal, neutrality condition and action mass law have been applied. Then, hole and electron concentrations and electro-static potential have been imposed as:

$$\Psi = V_a + \frac{kT}{q} ln\left[\frac{1}{N_i}\left(\frac{C}{2} + \sqrt{\left(\frac{C}{2}\right)^2 + N_i^2}\right)\right] \tag{10}$$

$$N_e = \frac{C}{2} + \sqrt{\left(\frac{C}{2}\right)^2 + N_i^2} \tag{11}$$

$$N_h = -\frac{C}{2} + \sqrt{\left(\frac{C}{2}\right)^2 + N_i^2} \tag{12}$$

where k is the Boltzmann constant and T = 300 K is the operating absolute temperature. By solving the coupled equations (10), (11) and (12) with given boundary conditions, both electro-static potential and free carrier distribution can be calculated in modulator cross section for any value of applied voltage, V_a. In Fig. 10, electro-static potential $\psi(x,y)$ for V_a=2 V is shown. Free electron distribution along the center of modulator cross section is shown in Fig. 11 for V_a varying in the range from 0 to 3 V. From simulations, flat band voltage has been estimated as equal to 1.45 V.

Starting from 2D free carrier distribution, silicon refractive index change Δn_{Si} as due to the applied voltage is calculated at each point of modulator cross section. Refractive index shift is related to free carrier distribution by well known Soref's relation at wavelength of 1550 nm (Soref & Bennett, 1987):

$$\Delta n_{Si} = -8.8\times10^{-22}\,\Delta N_e - 8.5\times10^{-18}\left[\Delta N_h\right]^{0.8} \tag{13}$$

where ΔN_e is the electron concentration change and ΔN_h is the hole concentration change (both in cm^{-3}). Using this approach, refractive index distribution $n(x,y)$ is found for any V_a value. In Fig. 12 refractive index distribution is sketched along the center of modulator cross section, for V_a ranging from 0 to 3 V.

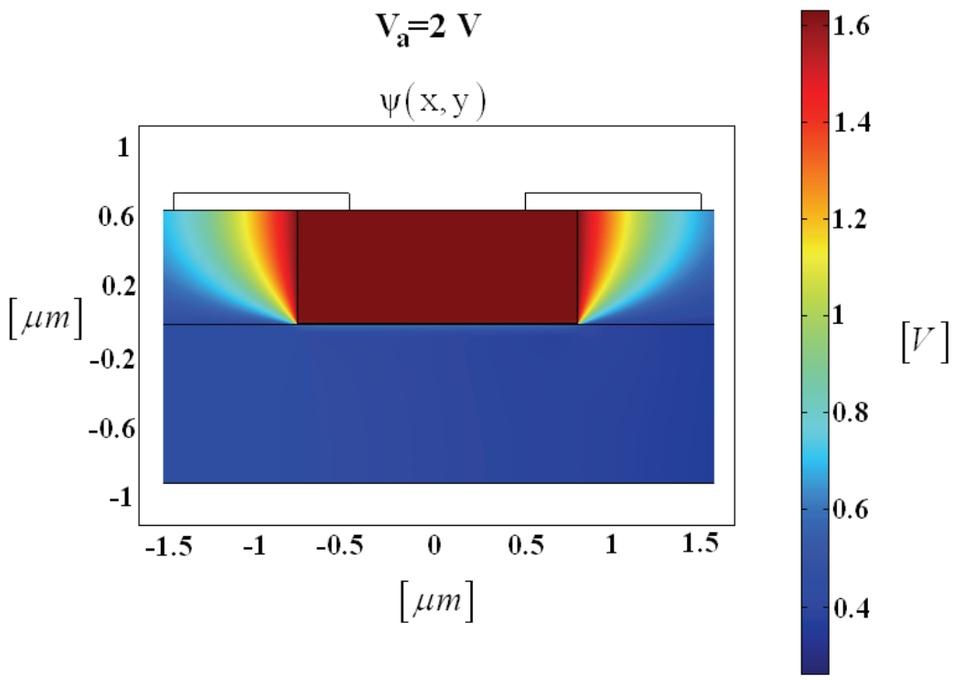

Figure 10. Electro-static potential for Va = 2 V

From knowledge of function $n(x,y,V_a)$, optical mode field distributions propagating within the device and their effective indices n_{eff} can be calculated as eigen-functions and eigenvalues of the optical wave equation (4). As an example, quasi-TE and quasi-TM mode electromagnetic field distributions have been calculated by FV-FEM and sketched in Fig. 13 and 14, respectively, for V_a = 2 V. Significant difference in quasi-TE and quasi-TM mode profiles are evident. Quasi-TE is more confined in the waveguide as compared to quasi-TM.

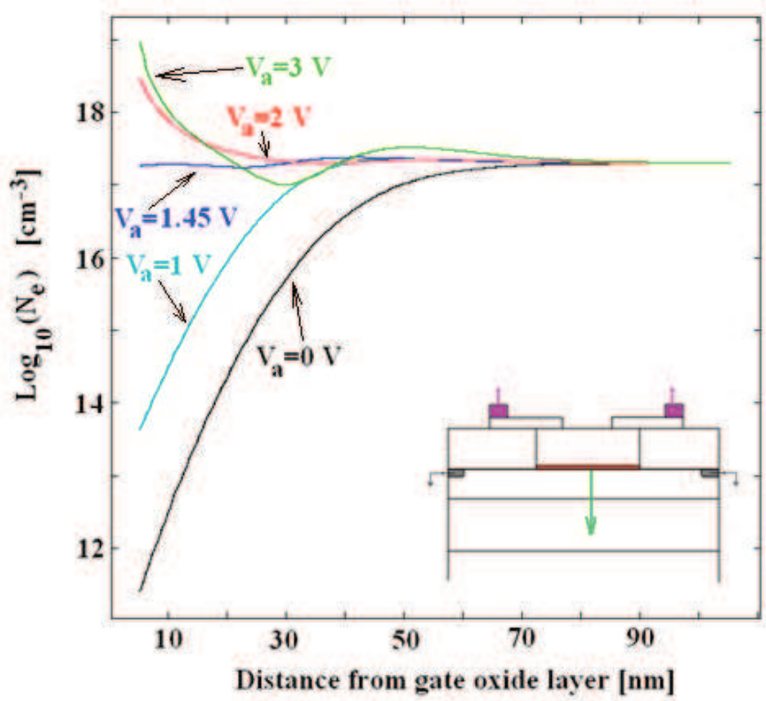

Figure 11. Electron distribution along the center of modulator cross section for Va ranging from 0 V to 3 V

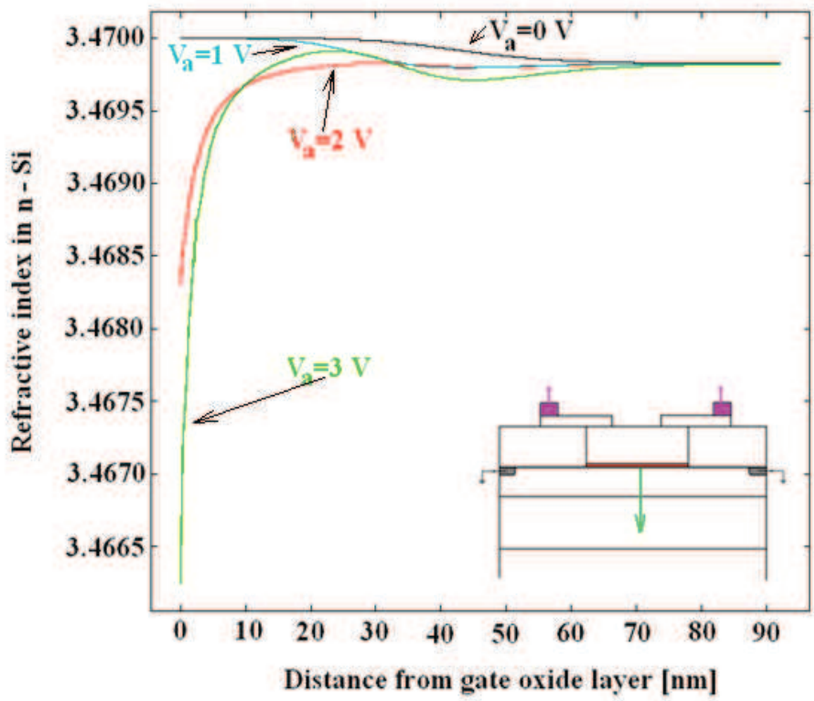

Figure 12. Refractive index distribution along the center of modulator cross section in n-doped silicon, for V_a ranging from 0 V to 3 V

This difference is due to the continuity condition of electric field x component, E_x, and discontinuity of electric field y component, E_y, across the interface between silicon and gate oxide. For quasi-TE mode, E_y is the minor electric field component, whereas for quasi-TM mode E_y is the major electric field component, then E_y discontinuity practically produces effects only on quasi-TM polarized light. Therefore, the MOS capacitor based phase-shifter performance is strongly dependent on the incoming light polarization.

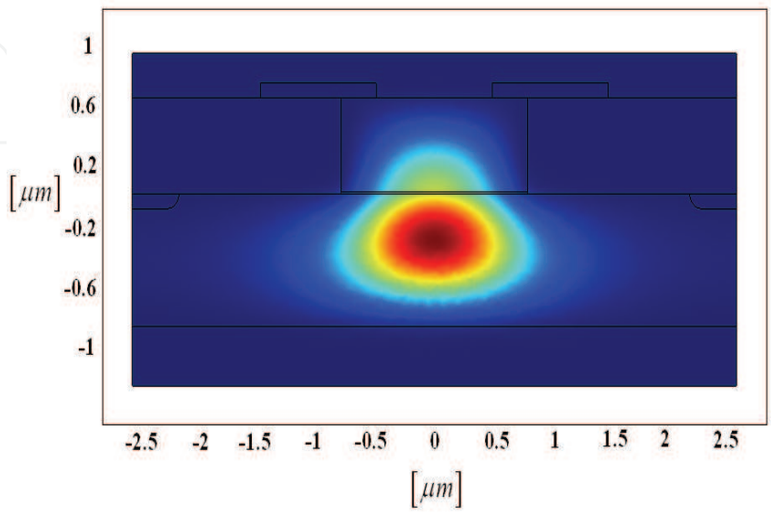

Figure 13. Quasi-TE mode electromagnetic field distribution for Va = 2 V

Phase shift induced in the optical signal propagating within the modulator and its dependence on applied voltage V_a have been investigated either for quasi-TE or quasi-TM mode, assuming a modulator length L = 8 mm (see Fig. 15). As expected, phase shift induced by an applied voltage change is significantly lower for quasi-TM polarized light (about 66% for L = 8 mm) than for quasi-TE. Through this calculation, a $V_\pi L$ product has been estimated as 3.4 V·cm for quasi-TE and 10.2 V·cm for quasi-TM polarized light.

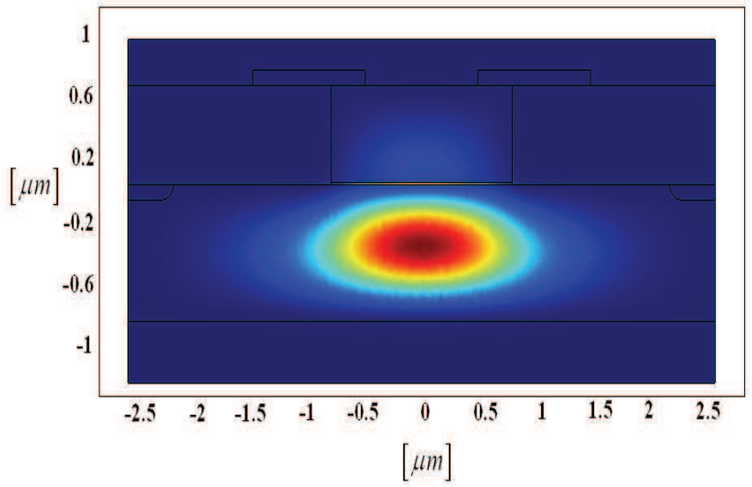

Figure 14. Quasi-TM mode electromagnetic field distribution for Va = 2 V

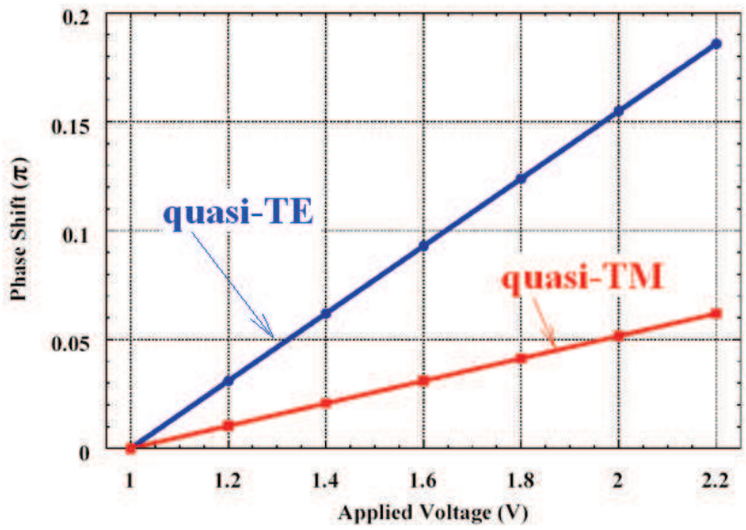

Figure 15. Phase shift induced in TE and TM-polarized light as a function of applied voltage

2.4. Nonlinear silicon photonic devices

Nowadays, there is a very strong interest in literature in investigating and developing silicon photonic devices for nonlinear applications. A number of significant devices have been presented and demonstrated, including Raman amplifiers and lasers (De Leonardis & Passaro, 2007). As a transmission medium, silicon has much higher nonlinear effects than the commonly used silicon dioxide, in particular the Raman effect. The crucial importance of both experimental and theoretical investigations on nonlinear effects in SOI waveguides has been recently demonstrated by a review paper (Lin et al., 2007).

To investigate all nonlinear effects involved in the propagation of ultrafast pulses in SOI rib waveguides, a very generalized modelling is often required (Passaro & De Leonardis, 2006). In fact, a large number of effects is to be taken into account, including two photon absorption (TPA), Free Carrier Absorption (FCA) where the free carriers are generated by TPA of the propagating pulse, plasma dispersion, Self-Phase-Modulation (SPM) as induced by the Kerr nonlinearity, Group-Velocity Dispersion (GVD), third-order dispersion (TOD), self steeping, intra-pulse Raman scattering, mode polarization effects. In this section, some modelling aspects on the formation and propagation of optical solitons in sub-picosecond regime in SOI optical waveguides are investigated, showing the role of a FEM-based approach.

When sub-picosecond optical pulses propagate inside a waveguide, both dispersive and nonlinear effects largely influence their shapes and spectra. Then, the equation system must also take into account a number of higher order nonlinear effects induced by the delayed Raman response. Thus, the nonlinear response function is influenced and, then, SPM effect. In addition, the introduction of this delayed response allows to extend the investigation for pulse time widths well below 1 ps, ranging from 10 to 1000 fs. The nonlinear response function $R(t)$ can be written as:

$$R(t) = (1 - f_R)\delta(t) + f_R h_R(t) \tag{14}$$

where $\delta(t)$ indicates the Dirac delta function and f_R represents the fractional contribution of the delayed Raman response to nonlinear polarization P_{NL}. Thus, $R(t)$ includes both electronic and vibrational (Raman) contributions. In addition, the Raman response function $h_R(t)$ is responsible for the Raman gain spectrum. Its functional form can be deduced from the Raman gain spectrum, $g_R(\Delta\omega)$, known to exhibit a Lorentzian shape. Fraction f_R is estimated from the numerical value of the Raman gain peak and normalization condition $\int h_R(t)dt = 1$. Assuming a gain peak value of 20 cm/GW (typical for silicon at λ = 1550nm), it results f_R = 0.043, well smaller than in silica fibers, i.e. 0.18. In the following analysis, we assume a typical SOI waveguide as sketched in Fig. 4, having rib total height h+R, slab height h, rib width w and air cover (without heater). In a single-mode SOI waveguide, two propagating modes are typically confined, one quasi-TE (dominant horizontal x-component of electric field) and one quasi-TM (dominant vertical y-component). Under the assumption of translational invariance along the propagation direction (z), the electric field in the single-mode SOI waveguide can be given in the form of variable separation, $E(x,y,z,t) = C \cdot F(x,y)\,A(z,t)e^{j\beta_0 z}$, where β_0 is the propagation constant, $F(x,y)$ is the optical mode distribution in the waveguide cross section $x-y$ (solutions of Helmoltz wave equation), and C is a normalization constant, $C = \left(\int_{-\infty}^{+\infty} \int |F(x,y)|^2 dxdy \right)^{-1/2}$. Thus, the total electric field inside the SOI waveguide can be written without any leak of generality as:

$$\mathbf{E}(x,y,z,t) = \hat{\mathbf{e}}\left[CA(z,t)F(x,y)e^{j(\beta_0 z - \omega t)} \right] \tag{15}$$

with the following meaning for the unit vector: $\hat{\mathbf{e}} = \hat{\mathbf{x}}$ for quasi-TE, or $\hat{\mathbf{e}} = \hat{\mathbf{y}}$ for quasi-TM mode, respectively. In Eq. (15), ω is the angular frequency of optical pulse injected into the SOI waveguide. Then, after some manipulations and assuming the nonlinear contributions to $\mathbf{P}_{NL}$ as a small perturbation of refractive index, we obtain the following differential equation for the propagating pulse:

$$\begin{aligned} &\frac{\partial A(z,t)}{\partial z} + \beta_1 \frac{\partial A(z,t)}{\partial t} + j\frac{1}{2}\beta_2 \frac{\partial^2 A(z,t)}{\partial t^2} - \frac{1}{6}\beta_3 \frac{\partial^3 A(z,t)}{\partial t^3} = \\ &= -\frac{\left(\alpha^{(prop)} + \alpha^{(FCA)}\right)}{2} A(z,t) - 0.5\beta^{(TPA)} f \left|A(z,t)\right|^2 A(z,t) + \\ &+ j\frac{2\pi}{\lambda}\Delta n A(z,t) + j\gamma\left(1 + \frac{j}{\omega}\frac{\partial}{\partial t}\right)\left[A(z,t) \cdot \int_{-\infty}^{+\infty} R(t')\left|A(z,t-t')\right|^2 dt' \right] \end{aligned} \tag{16}$$

which describes the time-space evolution of both quasi-TE or quasi-TM pulses. The coefficients β_1, β_2, β_3 indicate the group velocity, GVD and TOD coefficients, respectively.

Moreover, the term proportional to $\gamma = n_2 \omega f / c$ coefficient represents the SPM effect (due to Kerr nonlinearity), being c the light velocity and n_2 the nonlinear refractive index, while the term proportional to time derivative takes into account the self-steeping effect and the intrapulse Raman scattering. Moreover, $f^{-1} = A_{eff}$ represents the effective area of the optical mode for pulse injected into the SOI waveguide (calculated by FEM). Through coefficient $\beta^{(TPA)}$, the model includes the TPA effect as induced by the pulse propagation. Further, the total loss coefficient has been written as the summation of two contributions: $\alpha^{(prop)}$, the propagation loss coefficient in the rib waveguide, depending on the material absorption and fabrication process, and $\alpha^{(FCA)}$ the contribution due to FCA, as induced by the change of the free carriers generated mainly by TPA of the pulse. Finally, the term Δn represents the change of effective index due to the plasma dispersion effect as induced by the free carriers, whose dynamics being governed by the following rate equation:

$$\frac{dN_c}{dt} = -\frac{N_c}{\tau_{eff}} + \frac{\beta^{(TPA)}}{2\hbar\omega}\left(\left|A(z,t)\right|^2 f\right)^2 \tag{17}$$

where τ_{eff} is the relevant effective recombination lifetime for free carriers. The mathematical complexity of our model can be reduced without any leak of accuracy if we assume input pulse FWHM widths $T_{FWHM} \gg 10$ fs. In this case, the following approximated Taylor-series expansion holds:

$$\left|A_i(z,t-t')\right|^2 \cong \left|A(z,t)\right|^2 - t'\frac{\partial\left|A(z,t)\right|^2}{\partial t} \tag{18}$$

The previous relationship leads to avoid the integral term in Eq. (16). Then, by substituting Eq. (18) in (16), it becomes:

$$\begin{aligned} &\frac{\partial A(z,t)}{\partial z} + \beta_1\frac{\partial A(z,t)}{\partial t} + j\frac{1}{2}\beta_2\frac{\partial^2 A(z,t)}{\partial t^2} - \frac{1}{6}\beta_3\frac{\partial^3 A(z,t)}{\partial t^3} = \\ &= -\frac{\left(\alpha^{(prop)} + \alpha^{(FCA)}\right)}{2}A(z,t) - 0.5\beta^{(TPA)} f\left|A(z,t)\right|^2 A(z,t) + \\ &+ j\frac{2\pi}{\lambda}\Delta n A(z,t) + j\gamma\left(\left|A(z,t)\right|^2 A(z,t) + \frac{i}{\omega}\frac{\partial\left|A(z,t)\right|^2 A(z,t)}{\partial t} - T_R A(z,t)\frac{\partial\left|A(z,t)\right|^2}{\partial t}\right) \end{aligned} \tag{19}$$

where $T_R = f_R \left.\frac{d\tilde{h}_R}{d(\Delta\omega)}\right|_{\Delta\omega=0}$ governs the intrapulse Raman scattering. In the previous relationship, $\tilde{h}_R(\Delta\omega)$ represents the Fourier transform of the Raman response $h_R(t)$, which is directly related to the complex Raman gain through the Raman susceptibility. Assumption (18) allows to convert the equation system (16)-(17) in a partial differential equation system in the space-time domain (without using any integral term), solved by the

collocation method as a fast and accurate solution approach (Deb & Sharma, 1993). Hereinafter, normalized variables are used for numerical purposes, $U_i(z,t) = A_i(z,t)/\sqrt{P_0}$ and $\tau = (t - \beta_1 z)/T_0$, where P_0 is the Gaussian pulse peak power and T_0 is related to pulse FWHM width by $T_0 = T_{FWHM}/1.665$. Moreover, we will use normalized parameters to simplify the physical discussion, i.e. dispersion $L_D = T_0^2/|\beta_2|$, and nonlinear lengths $L_{NL} = 1/\gamma P_0$. To numerically solve the coupled equation system (17)-(19), the collocation method has been used by developing the unknown functions (A, N_c) as a linear combination of M orthogonal functions $\phi_m(\tau)$ through M weight functions $c_m(z)$. The algebraic details are presented in our previous work (Passaro & De Leonardis, 2006).

To test the mathematical model and the numerical method used to solve the equation system, we have compared our results with some numerical and experimental results presented in literature for propagation of sub-picosecond pulses in SOI. To the best of our knowledge, the first study involving ultrafast pulses in SOI waveguide has demonstrated the formation of solitons (Zhang et al., 2007). Thus, our general model has been applied to compare our results with that work. The SOI waveguide has rib total height $R+h$ = 400 nm, rib width w = 860nm and slab height h = 100 nm. Since the optical soliton can be obtained only in the anomalous GVD region, it is crucial to design the SOI waveguide to realise negative values of GVD coefficient. In this sense, our first comparison has involved the evaluation of the GVD coefficient spectrum for that waveguide. Simulations have been performed using the FV-FEM approach with about 60,000 elements mesh, and material dispersion considered by means of Sellmeier relationships. The following Table 4 shows the very good agreement with results in literature (Zhang et al., 2007).

Moreover, the model has been used to investigate the time-space evolution of ultrafast optical pulses. According with (Zhang et al., 2007), the quasi-TM ultrafast pulse is launched at λ = 1.484 μm with a Gaussian shape and FWHM width $T_{FWHM} = 116$ fs. The waveguide length is L = 5 mm, larger than both nonlinear and dispersion lengths. As a result, the interplay between SPM and GVD causes the pulses to evolve into a soliton. Fig. 16 shows the simulated shape of the output pulse by assuming $\beta^{(TPA)} = 0.45$ cm/GW, $n_2 = 6\times10^{-5}$ cm²/GW and $\alpha_i^{(prop)}$ = 5 dB/cm. In addition, the waveguide proposed has an anomalous GVD of -2.15 ps²/m for quasi-TM modes, as shown in Fig. 16.

Wavelength	β_2 (ps²/m) literature	β_2 (ps²/m) this work
λ = 1249 nm	0.81	0.83
λ = 1350 nm	-0.95	-0.92
λ = 1484 nm	-2.15	-2.10

Table 4. GVD coefficients for quasi-TM mode

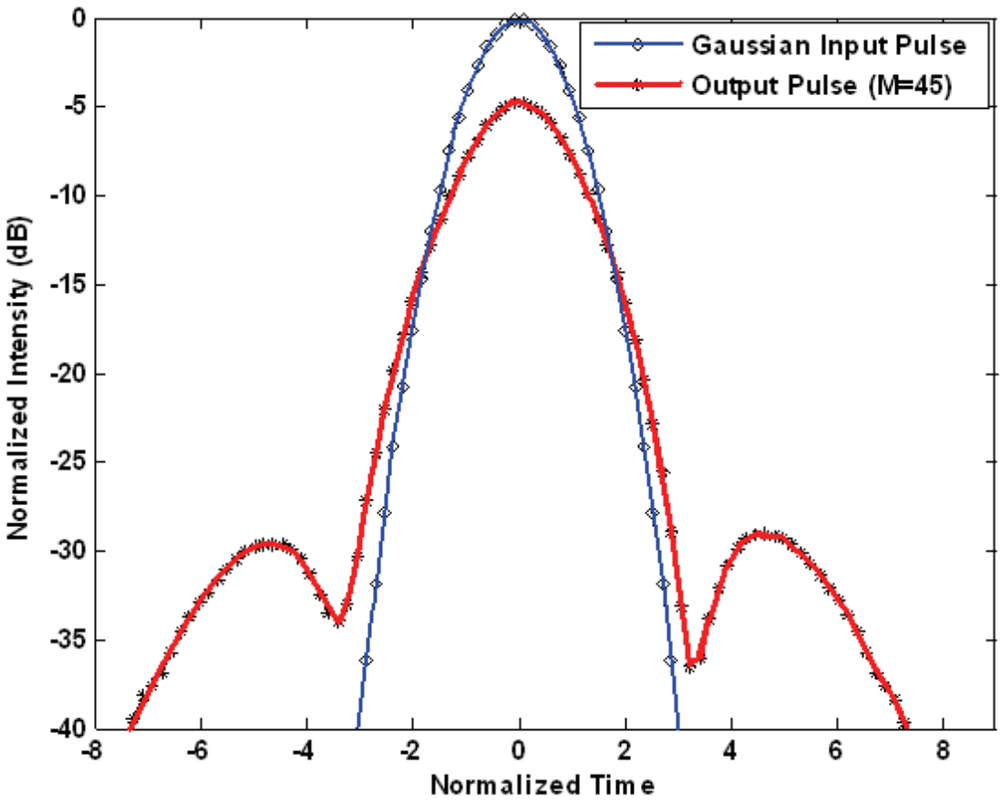

Figure 16. Normalized intensity versus normalized time for input and output pulses

According with data in literature, the input peak power has been selected to realise the condition $(L_D/L_{NL})^{1/2} \approx 1.35$. In the plot, the curve with diamond markers designates the input Gaussian pulse, while the curve with asterisk markers indicates the output pulse calculated with M = 45 collocation points. Then, a very good agreement with experimental results is demonstrated. The accuracy improves by increasing *M*, but this improvement is not significant for $M > 45$. Thus, $35 \le M \le 45$ represents the best trade-off between accuracy and calculation time. Moreover, by comparing the main lobes of input and output pulses, we see as the output pulse can be fitted by a *sech*-like pulse, confirming that the interplay between the SPM and GVD effects has caused the formation of the fundamental soliton.

In many applications, it is critical to find the design rules for any SOI rib waveguide to simultaneously meet single-mode and birefringence free conditions, or to achieve single-mode and zero GVD dispersion. Although the high refractive index contrast between the waveguide cladding and core makes easier the light confinement in submicron-scale structures, it also makes the control of waveguide birefringence extremely challenging. The research in birefringence control is driven primarily by the requirement of polarization insensitivity in interferometer devices such as arrayed waveguide gratings, ring resonators and all-optical devices, such as ultrafast switches and all-optical gates. It is well known that the waveguide core geometry influences not only the modal birefringence, but also other critical parameters, as the effective carrier recombination

lifetime τ_{eff}, GVD and TOD coefficients. Free carrier diffusion usually needs to be considered in addition to the recombination lifetime. In fact, if diffusion carriers move out of the modal area, this results in an effective lifetime shorter than the recombination lifetime in SOI structures. Usually a small cross section is necessary to obtain a low value for the carrier lifetime. However, it is known that the FCA induced by the TPA produces negligible effects for short pulses (< 1ps). Thus, the goal of waveguide design in sub-picosecond regime usually consists of the best trade-off between GVD and TOD effects.
A submicron structure with $R+h$ = 500 nm and $r = h/(R+h) = 0.2$ has been investigated for different values of rib width w and wavelength. A parametric plot of GVD coefficient spectrum for various w and both polarizations is sketched in Fig. 17 as achieved by FV-FEM.

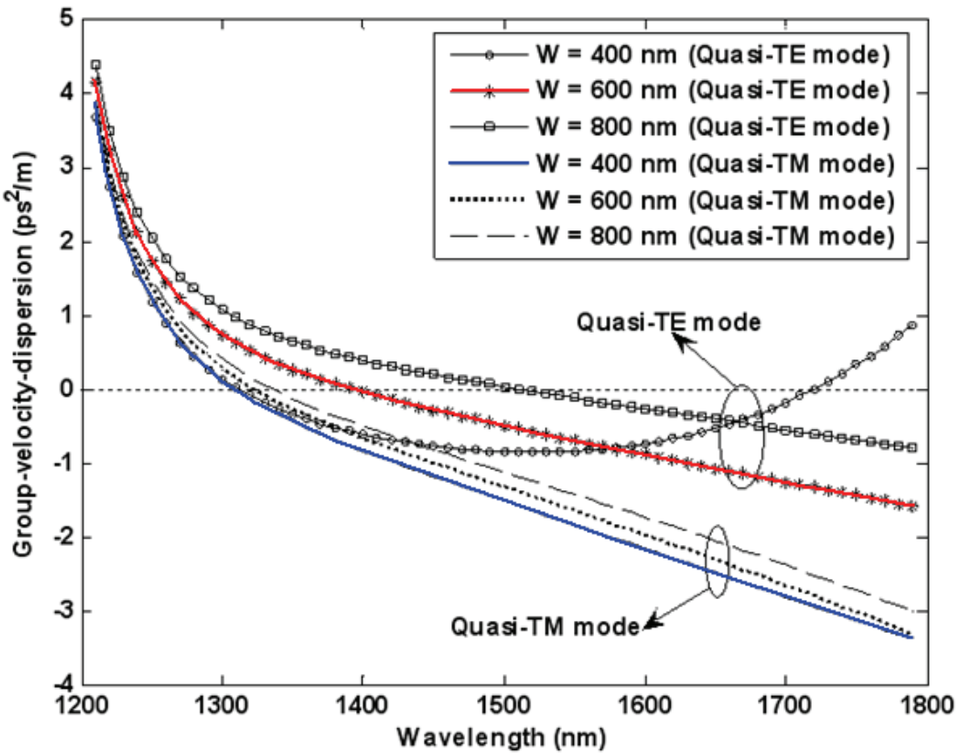

Figure 17. Group-velocity dispersion spectrum for different rib widths and both polarizations

Several features of this figure are noteworthy. In terms of values and shapes, quasi-TM modes show a smaller sensitivity than quasi-TE modes to rib width changes. In addition, for both polarizations it is possible to find the normal and anomalous dispersion regions. It is clear that β_2 spectrum shows a particular shape for quasi-TE polarization and w = 400 nm. This behaviour is explained considering that quasi-TM polarization is here the fundamental mode (approaching zero birefringence condition with increasing wavelength), differently from the other cases where the fundamental mode is quasi-TE. The plot in Fig. 18 shows the TOD coefficient spectrum for different values of rib width and both polarizations.

The plots indicate that, in the wavelength range 1200-1800 nm, quasi-TM modes have a β_3 larger than zero for each value of rib width. Same conclusions can be derived for quasi-TE modes except from the case w = 400 nm, where condition $\beta_3 = 0$ is satisfied at $\lambda = 1521.2$ nm.

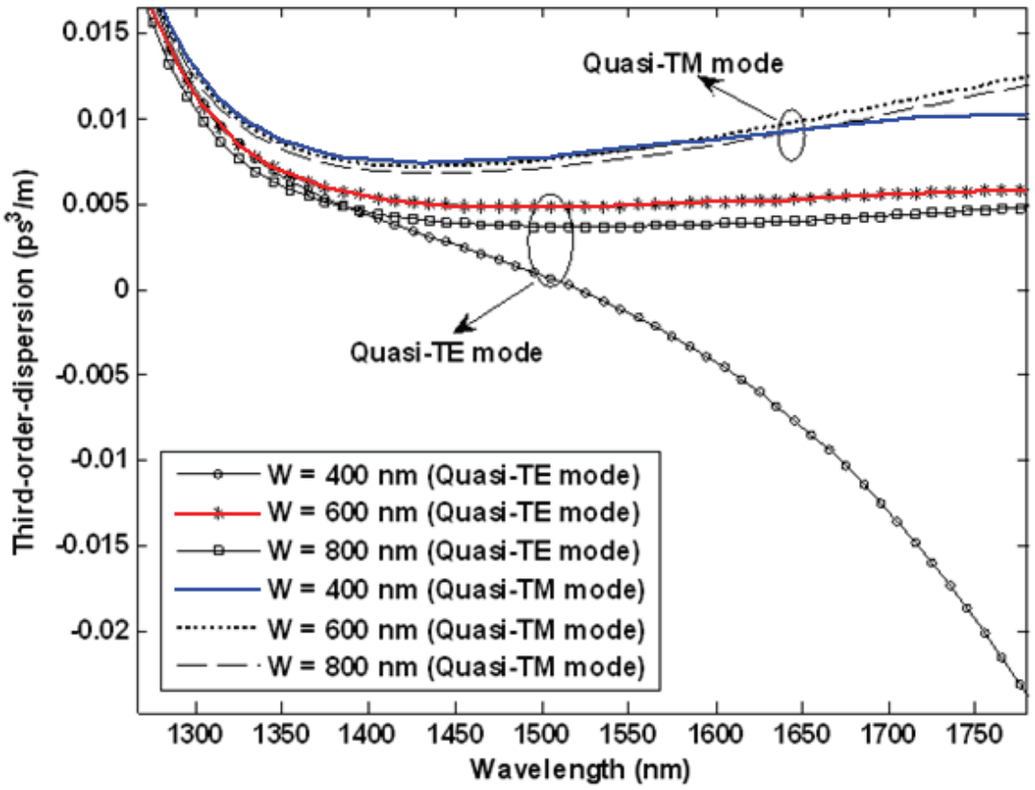

Figure 18. Third-order dispersion spectrum for different rib widths and both polarizations

3. Conclusion

This chapter briefly summarizes some important examples of modelling of photonic devices based on silicon technology. The potential, properties and advantages of finite element method-based modelling approaches are clearly presented and emphatized. Significant investigated devices include novel kinds of silicon optical waveguides (slot, hollow), thermo-optic modulated devices, plasma dispersion modulated devices (MOS modulators), as well as non linear silicon devices for generating optical solitons in SOI rib waveguides.

4. Acknowledgments

This work has been partially supported by Italian Ministry for University and Research under Interlink project, n. II04C01CDM. The authors wish to thank F. Dell'Olio and F. Magno for their valuable support.

5. References

Barrios, C. A. & Lipson, M. (2004). Modeling and analysis of high-speed electro-optic modulation in high confinement silicon waveguides using metal-oxide-semiconductor configuration. *Journal of Applied Physics*, Vol. 96, No. 11, 6008-6015, ISSN 0021-8979.

Deb, S. & Sharma, A. (1993). Nonlinear pulse propagation through optical fibers: an efficient numerical method. *Optical Engineering*, Vol. 32, No. 4, 695-699, ISSN 0091-3286.

De Leonardis, F. & Passaro, V. M. N. (2007). Modeling of Raman amplification in silicon-on-insulator optical microcavities, *New Journal of Physics*, Vol. 9, No. 2, 1-24, ISSN 1367-2630.

Dell'Olio, F. & Passaro, V. M. N. (2007). Optical sensing by optimized silicon slot waveguides. *Optics Express*, Vol. 15, No. 8, 4977-4993, ISSN 1094-4087.

Harrington, J. A. (2000). A Review of IR Transmitting, Hollow Waveguides. *Fiber and Integrated Optics*, Vol. 19, No. 3, 211-217, ISSN 0146-8030.

Lin, Q.; Painter, O. J. et al. (2007). Nonlinear optical phenomena in silicon waveguides: modeling and applications. *Optics Express*, Vol. 15, No. 25, 16604-16644, ISSN 1094-4087.

Muellner, P. & Hainberger, R. (2006). Structural Optimization of Silicon-on-Insulator slot Waveguides. *IEEE Photonics Technology Letters*, Vol. 18, No. 24, 2557-2559, ISSN 1041-1135.

Passaro, V. M. N. (2000). Optimal Design of Grating-Assisted Directional Couplers. *Journal of Lightwave Technology*, Vol. 18, No. 7, 973-984, ISSN 0733-8724.

Passaro, V. M. N. (2006). *Silicon Photonics*, Research Signpost Publ., ISBN 81-308-0077-2, Kerala (India).

Passaro, V. M. N. & De Leonardis, F. (2006). Space-Time Modeling of Raman Pulses in Silicon-on-Insulator Optical Waveguides. *Journal of Lightwave Technology*, Vol. 24, No. 7, 2920-2931, ISSN 0733-8724.

Reed, G. T. (2004). The optical age of silicon. *Nature*, Vol. 427, No. 6975, 595-596, ISSN 0028-0836.

Reed, G. T. & Knights, A.P. (2004). *Silicon Photonics: an introduction*, John Wiley and Sons, ISBN 0-470-87034-6, Chichester (UK).

Scarmozzino, R.; Gopinath, A. et al. (2000). Numerical Techniques for Modeling Guided-Wave Photonic Devices. *IEEE Journal of Selected Topics in Quantum Electronics*, Vol. 6, No. 1, 150-162, ISSN 1077-260X.

Soref, R. A. & Bennett, B. R. (1987). Electrooptical Effects in Silicon. *IEEE Journal of Quantum Electronics*, Vol. QE-23, No. 1, 123-129, ISSN 0018-9197.

Yamada, H.; Chu, T. et al. (2006). Si Photonic Wire Waveguide Devices. *IEEE Journal of Selected Topics in Quantum Electronics*, Vol. 12, No. 6, 1371-1379, ISSN 1077-260X.

Xu, Q.; Almeida, V. R. et al. (2004). Experimental demonstration of guiding and confining light in nanometer-size low refractive-index material. *Optics Letters*, Vol. 29, No. 14, 1626-1628, ISSN 0146-9592.

Zhang, J.; Lin, Q. et al. (2007). Optical solitons in silicon waveguides. *Optics Express*, Vol. 15, No. 12, 7682-7688, ISSN 1094-4087.

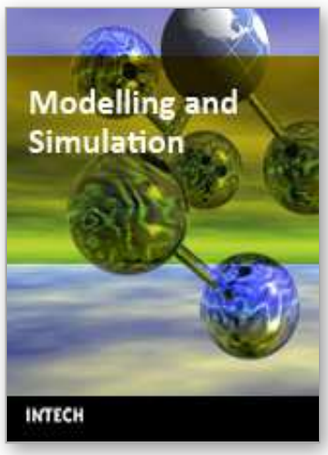

Modelling and Simulation

Edited by Giuseppe Petrone and Giuliano Cammarata

ISBN 978-3-902613-25-7
Hard cover, 688 pages
Publisher I-Tech Education and Publishing
Published online 01, June, 2008
Published in print edition June, 2008

This book collects original and innovative research studies concerning modeling and simulation of physical systems in a very wide range of applications, encompassing micro-electro-mechanical systems, measurement instrumentations, catalytic reactors, biomechanical applications, biological and chemical sensors, magnetosensitive materials, silicon photonic devices, electronic devices, optical fibers, electro-microfluidic systems, composite materials, fuel cells, indoor air-conditioning systems, active magnetic levitation systems and more. Some of the most recent numerical techniques, as well as some of the software among the most accurate and sophisticated in treating complex systems, are applied in order to exhaustively contribute in knowledge advances.

How to reference

In order to correctly reference this scholarly work, feel free to copy and paste the following:

Vittorio M. N. Passaro and Francesco De Leonardis (2008). Recent Advances in Modelling and Simulation of Silicon Photonic Devices, Modelling and Simulation, Giuseppe Petrone and Giuliano Cammarata (Ed.), ISBN: 978-3-902613-25-7, InTech, Available from: http://www.intechopen.com/books/modelling_and_simulation/recent_advances_in_modelling_and_simulation_of_silicon_photonic_devices

INTECH
open science | open minds

InTech Europe
University Campus STeP Ri
Slavka Krautzeka 83/A
51000 Rijeka, Croatia
Phone: +385 (51) 770 447
Fax: +385 (51) 686 166
www.intechopen.com

InTech China
Unit 405, Office Block, Hotel Equatorial Shanghai
No.65, Yan An Road (West), Shanghai, 200040, China
中国上海市延安西路65号上海国际贵都大饭店办公楼405单元
Phone: +86-21-62489820
Fax: +86-21-62489821

IntechOpen